



Contents lists available at ScienceDirect

Science Bulletin

journal homepage: www.elsevier.com/locate/scib

Article

Disentangling perovskite surface work functions and electron extraction energy offsets to drive high photovoltaic efficiency

Shaobing Xiong^{a,b,1}, Di Li^{a,1}, Junhan Xie^c, Hongbo Wu^d, Zaifei Ma^d, Bo Li^a, Xianjie Liu^e, Mats Fahlman^{e,*}, Junhao Chu^b, Caofeng Pan^{f,g,*}, Qinye Bao^{a,h,*}

^a School of Physics and Electronic Science, East China Normal University, Shanghai 200241, China

^b Shanghai Frontiers Science Research Base of Intelligent Optoelectronics and Perception, Institute of Optoelectronics, Fudan University, Shanghai 200433, China

^c School of Physical Science and Technology, ShanghaiTech University, Shanghai 201210, China

^d Center for Advanced Low-Dimension Materials, Donghua University, Shanghai 201620, China

^e Laboratory of Organic Electronics, Linköping University, Norrköping, 60174, Sweden

^f Institute of Atomic Manufacturing, Beihang University, Beijing 100191, China

^g International Research Institute for Multidisciplinary Science, Beihang University, Beijing 100191, China

^h Collaborative Innovation Center of Extreme Optics, Shanxi University, Taiyuan 030006, China

ARTICLE INFO

Article history:

Available online xxx

Keywords:

Work function

Energy offset

Nonradiative recombination

Charge transport

Perovskite solar cell

ABSTRACT

Reducing nonradiative recombination is a main challenge in manufacturing highly efficient optoelectronic devices. Perovskite solar cells (PSCs) typically feature significant nonradiative recombination originating from energetic mismatch at the charge-extracting contact. Here, we widely manipulate the energy offset between the perovskite conduction band minimum (CBM) and the electron transporting state of the fullerene cathode interface layer in p-i-n PSCs by modifying the perovskite surface work function with defect-passivating self-assembled monolayers (SAMs) inducing surface dipoles. It is found that reducing the energy offset for electron extraction at such perovskite/fullerene electron-selective heterointerface from 0.98 to -0.02 eV yields a clear linear improvement in PSC built-in potential, with fill factor, photovoltage and power conversion efficiency all increasing as well. We further demonstrate that the improved photovoltaic performance is attributed to reduced energy offsets between the perovskite CBM and the fullerene electron accepting state, which accelerates electron extraction from perovskite and thus effectively suppresses nonradiative recombination. Moreover, the models of corresponding energy level alignment are proposed to discuss the impacts on PSC performance. Our work highlights the importance of tuning the work function even for defect-passivated perovskite surfaces to achieve barrier-less charge extraction and thus boost PSC performance.

© 2025 The Authors. Published by Elsevier B.V. and Science China Press. All rights are reserved, including those for text and data mining, AI training, and similar technologies.

1. Introduction

Metal halide perovskite is an excellent class of semiconductors for optoelectronic devices, e.g., lighting-emitting diodes, solar cells, and photodetectors, due to its high absorption coefficients, low exciton binding energies, long carrier diffusion lengths, adjustable band gaps and low-temperature processing capabilities [1–6]. Perovskite solar cells (PSCs) are a particularly promising next-generation photovoltaic technology, exhibiting an increase in

power conversion efficiencies (PCEs) that outperform those of other conventional thin-film cells (<https://www.nrel.gov/pv/cell-efficiency.html>). Nevertheless, PSCs still suffer from severe nonradiative recombination losses primarily at the heterointerface between the perovskite and the electrode charge transport interlayers, leading to a significant gap between the state-of-the-art PCE and the Shockley-Queisser (S-Q) theoretical limit [7–9].

For a multilayer-structured device, the heterointerfaces in PSC influence the device's power output by governing charge transport dynamics, in which charge extraction, accumulation and recombination have all been demonstrated as heterointerface-energetics-dominated processes [10–12]. The heterointerface energetics should be designed to boost majority carrier transport while blocking minority carriers, thereby suppressing interfacial nonradiative

* Corresponding authors.

E-mail addresses: mats.fahlman@liu.se (M. Fahlman), pancaofeng@buaa.edu.cn (C. Pan), qybao@clpm.ecnu.edu.cn (Q. Bao).

¹ These authors contributed equally to this work.

<https://doi.org/10.1016/j.scib.2025.03.034>

2095-9273/© 2025 The Authors. Published by Elsevier B.V. and Science China Press. All rights are reserved, including those for text and data mining, AI training, and similar technologies.

recombination. This will result in efficiency gain, particularly in terms of enhanced open-circuit voltage (V_{oc}) and fill factor (FF) [13–16]. For inverted p-i-n PSCs that have advantages in stability and compatibility with integration into tandem structural cells [17,18], the buried perovskite/anode hole transport layer heterointerface energetics can be optimized using self-assembled monolayers (SAMs) with defect-passivation anchoring groups [19–21]. However, the top heterointerface between the perovskite and the cathode electron transport layer, the latter normally made from fullerene and its derivatives, features significant nonradiative recombination that originates from minority carriers in the vicinity of the heterointerface [22,23].

Much efforts has been invested in developing protocols for passivating perovskite top surface defects to reduce the nonradiative recombination in p-i-n PSCs, often employing thin layers of surfactants [24–26]. However, nonradiative recombination at the electron-extracting heterointerface also suggests a significant energy mismatch and hence an electron-extraction barrier between the perovskite conduction band minimum (CBM) and the electron accepting state of the electron transport layer, hereafter referred to as the lowest unoccupied molecular orbital (LUMO), following common nomenclature. An electron-extraction barrier will significantly affect device's V_{oc} and FF. To eliminate such energetic mismatch, and thereby enhance electron extraction efficacy and suppress nonradiative recombination, it is essential to reconstruct and optimize the energy level alignment at perovskite heterointerfaces for promoting PSC performance. However, this remains an ongoing challenge.

In this work, we functionalize the perovskite surface work functions (WFs) by forming positive and negative dipoles to widely manipulate the interfacial energetics, specifically the CBM-LUMO energy offsets ($\Delta E_{CBM-LUMO}$) between the perovskite's CBM and the electron transport material's LUMO for p-i-n PSCs and explore their correlation with PSC performance. Reducing $\Delta E_{CBM-LUMO}$ yields increasing PSC performance, where the resulting PCE improves from 11.20% to 24.36% by decreasing the $\Delta E_{CBM-LUMO}$ from 0.98 to -0.02 eV. Furthermore, we demonstrate that a matched energetic with \sim zero $\Delta E_{CBM-LUMO}$ can significantly improve band alignment and promote electron extraction from perovskite to PCBM, suppressing nonradiative recombination. In contrast, a large $\Delta E_{CBM-LUMO}$ reduces the electron selectivity at the electron-selective contact, causing severe losses in V_{oc} and FF. This work highlights the efficacy of using defect-passivating dipole layers that effectively tune the perovskite surface WFs to achieve barrier-less electron extraction and minimize nonradiative losses for developing highly efficient perovskite solar cells.

2. Materials and methods

2.1. Materials

Lead iodide (PbI_2), lead bromide ($PbBr_2$), cesium iodide (CsI) and bathocuproine (BCP) were received from Xi'an Polymer Light Technology Corp. Formamidinium iodide (FAI), methylammonium bromide (MABr), methylamine hydrochloride (MACl) and [6,6]-PhenylC61 butyric acid methyl ester (PCBM) were purchased from Advanced Election Technology Co. Ltd. [2-(3,6-dimethoxy-9H-carbazol-9-yl)ethyl]phosphonic acid (MeO-2PACz), 4-Nitrobenzoic Acid ($BA-NO_2$), 4-Methoxybenzoic Acid ($BA-OCH_3$), 4-Hydroxyphenylphosphonic Acid (PA-OH) and 4-Methoxyphenylphosphonic Acid ($PA-OCH_3$) were obtained from TCI America. Dimethylformamide (DMF), dimethyl sulfoxide (DMSO), chlorobenzene (CB), isopropanol (IPA) and ethanol were purchased from Sigma Aldrich. All materials are used as received.

2.2. Device fabrication and characterization

Indium-tin oxide (ITO) patterned glass was cleaned sequentially by detergent, ultra-pure water, ethanol, and isopropanol under ultrasonication for 15 min. The cleaned ITO was treated by UV-ozone for 20 min before use and then transferred to a nitrogen-filled glove box. The solution of MeO-2PACz (0.5 mg mL^{-1} in ethanol) as hole transport layer was deposited on ITO at 5000 r min^{-1} for 30 s, followed by annealing at $100 \text{ }^\circ\text{C}$ for 10 min. The perovskite precursor (1.3 mol L^{-1}) with a formula of $Cs_{0.05}(FA_{0.95}MA_{0.05})_{0.95}Pb(I_{0.95}Br_{0.05})_3$ was prepared by mixing PbI_2 , $PbBr_2$, FAI, MABr, and CsI in DMF/DMSO (4:1 in v/v) mixed solvent according to the stoichiometric ratio, with an additional 30 mol% MACl. The perovskite precursor was spin-coated on MeO-2PACz at 4000 r min^{-1} for 40 s, and $200 \text{ } \mu\text{L}$ CB was dropped on the film at 7 s before the end of the spin-coating process, followed by annealing at $100 \text{ }^\circ\text{C}$ for 30 min. The dipole molecules including $BA-NO_2$ (5 and 8 mg mL^{-1} in ethanol), $BA-OCH_3$ (5 mg mL^{-1} in ethanol), $PA-OH$ (5 mg mL^{-1} in ethanol), and $PA-OCH_3$ (5 mg mL^{-1} in ethanol) were deposited on the perovskite film at 4000 r min^{-1} for 30 s and annealed at $100 \text{ }^\circ\text{C}$ for 10 min. Then PCBM (20 mg mL^{-1} in CB) as electron transport layer was spin-coated at 1800 r min^{-1} for 40 s. After that, BCP (0.5 mg mL^{-1} in IPA) was dynamically deposited on PCBM at 6000 r min^{-1} for 30 s. Finally, 100 nm Ag was thermally evaporated under high vacuum ($< 2 \times 10^{-4} \text{ Pa}$). The device active area was defined as 0.05 cm^2 by metal shadow mask.

Device current-voltage (J - V) curves were measured by using Keithley 2400 system and a solar simulator (SS-F5-3A, Enlitech) in the N_2 -filled glovebox without any preconditioning. The light intensity (AM 1.5G, 100 mW cm^{-2}) was calibrated with an NREL-certified Si cell (KG-2) to keep the spectral mismatch correction at 1.00 ± 0.01 , and the measurement proceeded with a scan rate of 0.1 V s^{-1} , a voltage step of 0.02 V , and a delay time of 10 ms. Capacitance-voltage (C - V) curves were obtained from an impedance spectroscopy (PGSTAT302N, Autolab) at a frequency of 5 kHz . The external quantum efficiency of electroluminescence (EQE_{EL}) spectra was recorded by a Kymera-3281 spectrograph and a Si EMCCD camera (DU970PBVF, Andor). A digital source meter (Keithley 2400) was used to inject current into perovskite solar cell, and a picometer (Keithley 6482) with a Si photodiode was employed to quantify the photons emitted from device.

2.3. Film characterization

X-ray diffraction (XRD) patterns were carried out by a PANalytical X-ray diffractometer (D8 DISCOVER, Bruker) with $Cu K\alpha$ radiation. UV-visible absorption spectra were recorded by a UV-vis-NIR spectrometer (TU-1901). Steady-state photoluminescence (PL) and time-resolved photoluminescence (TRPL) measurements were performed via a time-corrected single photon counting (TCSPC) system with an excitation wavelength of 450 nm , where the film samples were coated on ITO glass.

2.4. Photoelectron spectroscopy measurement

Ultraviolet photoelectron spectroscopy (UPS) measurements were carried out in an ultrahigh vacuum surface analysis system (base pressure $\approx 10^{-10} \text{ mbar}$) equipped with a Scienta-R3000 spectrometer. A monochromatic He I light source (21.22 eV) was employed as the excitation source with an energy resolution of 50 meV . The work function and valence band maximum were derived from the secondary electron cutoff and the frontier edge of the occupied density of states relative to vacuum level, respectively. All spectra were calibrated by referencing to Fermi level

and Au 4 $f_{7/2}$ position of the Ar⁺ ion sputter-cleaned Au foil, and Fermi level was referred as the zero binding energy.

2.5. Femtosecond transient absorption (fs-TA) spectroscopy measurement

Fs-TA measurements were performed via a commercial femtosecond TA spectrometer (HELIOS, Ultrafast System), and the source pulse laser (800 nm, 35 fs, 1 kHz) was provided by a Ti: sapphire laser (Coherent, Astrella). The pump pulse with a central wavelength of 515 nm was generated through an optical parametric amplifier (OPerA Solo, Coherent Inc), and the probe beam was a broadband supercontinuum white light of 480–770 nm. The pump and probe pulses were focused on the films with an overlapping spot diameter of 100 μm . The time constant of the instrument response function (IRF) was about 120 fs. The film samples were coated on ITO glass for fs-TA measurements.

3. Results and discussion

3.1. Tuning perovskite surface WFs by dipoles

We tune the surface WF of the perovskite films over a wide range by depositing self-assembled monolayer (SAM) molecules with intrinsic molecular dipole moments [27]. As depicted in Fig. 1a, a surface dipole moment pointing out from the perovskite surface (referred to as a “negative dipole”) will bring an abrupt downward shift of the vacuum level (VL) at the surface, leading to a low-WF perovskite. In contrast, a surface dipole moment pointing toward the perovskite surface (referred to as a “positive dipole”) will shift the vacuum level upwards and thus form a high-WF perovskite. Note that the perovskite bulk chemical potential is not changed by this treatment. Fig. 1b shows the chemical structures of the SAM molecules employed to functionalize the perovskite surface energetics: 4-Nitrobenzoic Acid (BA-NO₂), 4-Methoxybenzoic Acid (BA-OCH₃), 4-Hydroxyphenylphosphonic Acid (PA-OH) and 4-Methoxyphenylphosphonic Acid (PA-OCH₃). Here, the SAM anchoring groups are carefully chosen to provide similar defect-passivating functionality enabling us to selectively explore the influence of $\Delta E_{\text{CBM-LUMO}}$ on electron extraction and overall device performance.

We conduct ultraviolet photoelectron spectra (UPS) measurements to investigate the impact of the SAMs on the perovskite surface energetics, where the WFs are extracted from the secondary electron cutoff (right panel of Fig. 1c) and the valence band maximum (VBM) positions relative to the Fermi level (E_{F}) from the frontier energy level onset in a logarithmic photoemission intensity scale (left panel of Fig. 1c). The pristine perovskite has a moderate WF of 4.48 eV and a VBM relative to E_{F} of 1.12 eV, resulting in an ionization potential (IP) of 5.60 eV. As the bandgap of the perovskite photoactive layer is 1.55 eV, the CBM is estimated to be 4.05 eV. The WF of the SAM-modified perovskite decreases to 4.35 and 4.16 eV due to the negative surface dipoles induced by PA-OH and PA-OCH₃, respectively. BA-OCH₃ and BA-NO₂ generate positive dipoles on the perovskite surface, leading to increased WFs of 4.70, 4.91 and 5.18 eV, respectively, where the highest WF is reached for BA-NO₂ SAMs deposited at higher concentrations. Fig. 1d summarizes the WF shift of the perovskite surface by SAM-induced dipole layers (ΔE_{dip}), where a broad range shift from -0.32 to 0.70 eV was achieved. It is noted that the thin SAM treatment has a negligible effect on the perovskite crystallinity and optical properties (Figs. S1, S2 online).

3.2. Determining energy offsets at electron-selective contact

Inverted p-i-n planar PSC with a common configuration of ITO/MeO-2PACz/Perovskite/Dipole layer/PCBM/BCP/Ag is employed in this study (Fig. 2a), where PCBM serves as the capping electron transport layer. To understand the energetics at the perovskite/PCBM heterointerface, we first carried out UPS measurements to map the PCBM pinning energies according to ICT model (Fig. 2b and Figs. S3, S4 online) [28]. The WF of PCBM represents a typically “Mark of Zorro”-type dependence on the WF of bare substrates, where the negative pinning energy ($E_{\text{ICT-}}$) and positive pinning energy ($E_{\text{ICT+}}$) for PCBM are 4.17 and 5.17 eV, respectively, which are comparable with the previous report [29,30]. Hence, the UPS-derived energetics at the pristine and SAM-modified perovskite-PCBM junctions all occur in the so-called vacuum level alignment regime, with only the respective end points slightly modified by the PCBM pinning energies (5.18 eV > 5.17 eV and 4.16 eV < 4.17 eV). Fig. 2c shows the energy level alignments at perovskite/PCBM heterointerfaces with different dipoles, where the $\Delta E_{\text{CBM-LUMO}}$ between the perovskite’s CBM and the PCBM’s LUMO defines the barrier for electron extraction at the contact. The effective $\Delta E_{\text{CBM-LUMO}}$, taking into account the vacuum level shifts at the heterointerface, then decreases from 0.98 to -0.02 eV with the reduction of the perovskite surface WF, thus yielding an in-fact barrier-less contact for the perovskite modified by PA-OCH₃.

To evaluate the effect of $\Delta E_{\text{CBM-LUMO}}$ on charge transfer dynamics at the perovskite/PCBM heterointerface, we perform steady-state photoluminescence (PL) and time-resolved PL (TRPL) spectra measurements, as a decreased $\Delta E_{\text{CBM-LUMO}}$ should yield decreased charge carrier lifetimes. The PL intensity gradually decreases by reducing the $\Delta E_{\text{CBM-LUMO}}$ from 0.98 to -0.02 eV (Fig. S5 online), where the SAM-functionalized perovskite heterointerface with \sim zero $\Delta E_{\text{CBM-LUMO}}$ (-0.02 eV) features the strongest PL quenching, while the SAM-functionalized perovskite heterointerface with the largest $\Delta E_{\text{CBM-LUMO}}$ (0.98 eV) shows the weakest PL quenching. The corresponding charge carrier lifetime decreases from the 0.98 eV $\Delta E_{\text{CBM-LUMO}}$ heterointerface ($\tau_1 = 2.45$ ns, $\tau_2 = 10.70$ ns) to the -0.02 eV $\Delta E_{\text{CBM-LUMO}}$ heterointerface ($\tau_1 = 1.21$ ns, $\tau_2 = 4.43$ ns), which confirms that reduction of $\Delta E_{\text{CBM-LUMO}}$ significantly promote electron extraction from perovskite to PCBM and thus significantly suppresses nonradiative recombination (Fig. S6 and Table S1 online). As all the SAM molecules have -COOH or -POOH groups that have a similar defect-passivation effect on perovskite surfaces, we conclude that the observed differences in charge transfer dynamics at the perovskite/PCBM heterointerface are mainly attributed to the variation in $\Delta E_{\text{CBM-LUMO}}$.

3.3. Correlation between photovoltaic parameters and energy offsets

To further illustrate the impact of $\Delta E_{\text{CBM-LUMO}}$ on PSC performance, Fig. 3a exhibits the current density-voltage (J - V) curves of the resulting p-i-n PSCs with different dipole layers under a solar simulator with AM 1.5 G light illumination of 100 mW cm⁻². Their photovoltaic parameters are summarized in Table S2 (online). The pristine device has a comparable PCE of 21.39% with a V_{oc} of 1.082 V, a J_{sc} of 24.42 mA cm⁻² and an FF of 80.95%. When forming surface negative dipoles, the devices with PA-OH and PA-OCH₃ exhibit remarkably improved PCEs to 22.71% and 24.36%, accompanied by enhancements in V_{oc} of 1.111 and 1.158 V, J_{sc} of 24.59 and 24.83 mA cm⁻², and FF of 83.11% and 84.71%, respectively. Nevertheless, when forming surface positive dipoles, the devices with BA-OCH₃ and BA-NO₂ undergo dramatic performance collapse with diminished PCEs to 19.58%, 14.06% and 11.20%, respectively.

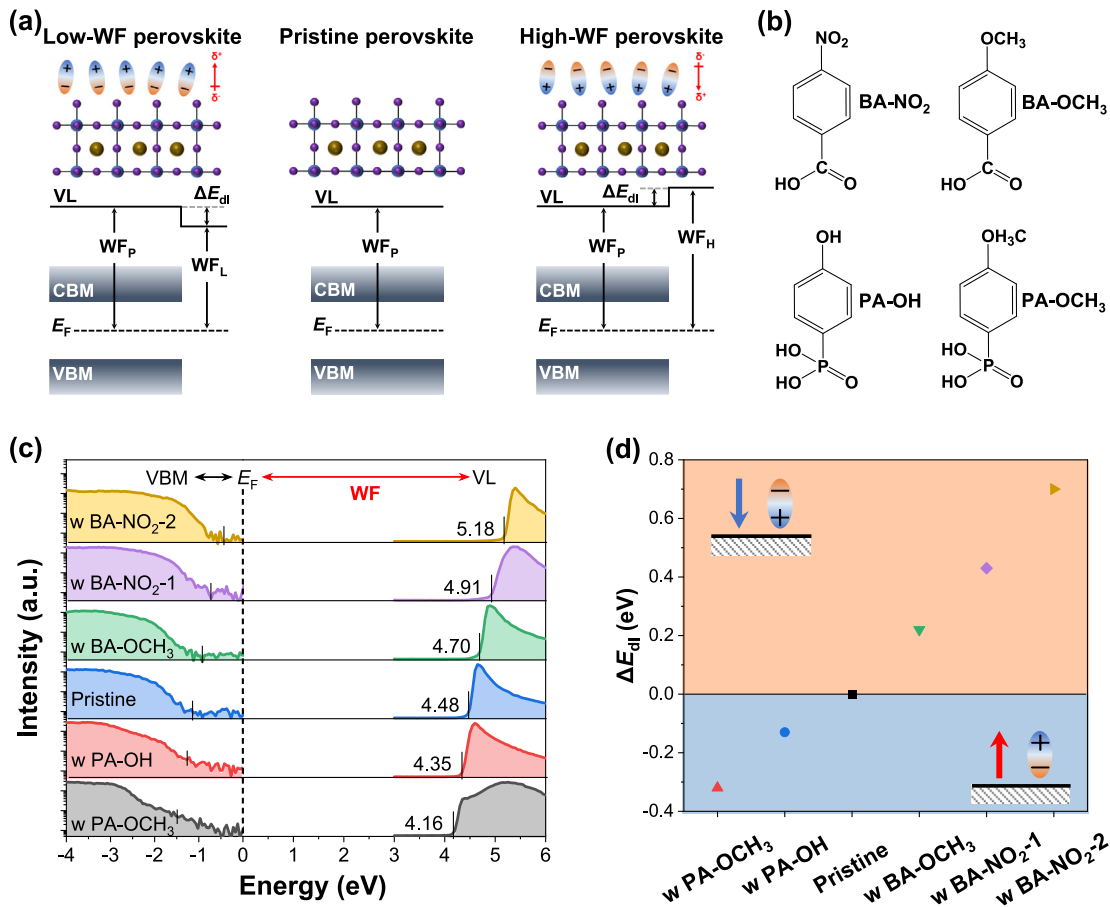


Fig. 1. (a) Representation of positive and negative dipole on perovskite surface, and its effect on WF and VL. (b) Chemical structures of SAM dipole molecules. (c) UPS spectra of pristine perovskite and modified perovskite with different dipole layers. (d) Summarized WF shift of perovskite surface induced by dipole layer (ΔE_{dip}).

Fig. 3b shows the evolutions of $\Delta E_{\text{CBM-LUMO}}$ with different surface dipole layers. The correlation between photovoltaic parameters (V_{oc} , J_{sc} , FF and PCE) and $\Delta E_{\text{CBM-LUMO}}$ is established in Fig. 3c–f. All photovoltaic parameters of the PSCs drastically increase with decreased $\Delta E_{\text{CBM-LUMO}}$. When the $\Delta E_{\text{CBM-LUMO}}$ is \sim zero (-0.02 eV), i.e., barrier-less electron extraction from the perovskite's CBM to the PCBM's LUMO, the PSCs achieve the highest PCE of 24.36%. When $\Delta E_{\text{CBM-LUMO}}$ is as large as 0.98 eV, the PSCs show a PCE of only 11.20% (despite also having a defect-passivated perovskite top surface through the SAM anchoring group -COOH). We attribute the enhanced V_{oc} to the reduced $\Delta E_{\text{CBM-LUMO}}$ at the perovskite/PCBM heterointerface, where both electron selectivity and transfer efficacy are greatly augmented when the perovskite's CBM aligns with the PCBM's LUMO. The improvement in FF is ascribed to enhanced electron extraction achieved by decreased series resistance at the contact. The poor device efficiency at large $\Delta E_{\text{CBM-LUMO}}$ originates from the joint collapse of V_{oc} , FF and J_{sc} . The mismatched interface energetics at the perovskite/PCBM heterointerface trigger severe nonradiative recombination, causing significant charge carrier losses that reduce J_{sc} as well as V_{oc} and FF.

3.4. Nonradiative recombination in p-i-n PSCs

To gain more insight into the influence of $\Delta E_{\text{CBM-LUMO}}$ on device performance, we carry out capacitance-voltage (C-V) plots to extract the built-in potential (V_{bi}) of the PSCs in Fig. 4a according to the Mott-Schottky equation: $\frac{1}{C^2} = \frac{2(V_{\text{bi}} - V)}{A^2 e \epsilon_0 N_A}$ (where A is device area,

ϵ is relative permittivity, ϵ_0 is vacuum permittivity, and N_A is carrier concentration) [31]. We find that there is a linear relationship between the decrease in $\Delta E_{\text{CBM-LUMO}}$ and the increase in V_{bi} (Fig. 4b), and the enhanced V_{bi} agrees with the increased V_{oc} of the PSCs. The larger V_{bi} promotes electron extraction at the perovskite/PCBM heterointerface while driving holes away from the interface region. The opposite effect will occur at the anode side, thereby decreasing interfacial charge recombination at both contacts. Fig. 4c displays V_{oc} versus light intensity (P) curves of the devices using the equation: $V_{\text{oc}} = \frac{nkT}{q} \ln(P)$ (where n is ideality factor, k is Boltzmann constant, T is absolute temperature, and q is elementary charge) [32]. The PSCs show a progressively decreasing slope from 1.95 to 1.40 in terms of kTq^{-1} , revealing that the nonradiative recombination is effectively suppressed by reducing $\Delta E_{\text{CBM-LUMO}}$.

We conduct analysis of the photovoltage loss and FF loss for PSCs with different $\Delta E_{\text{CBM-LUMO}}$. Fig. 4d shows the PSC external quantum efficiencies of electroluminescence (EQE_{EL}) operating as light-emitting diodes. The nonradiative recombination induced V_{oc} loss ($\Delta V_{\text{nonrad oc}}$) is quantitatively calculated according to the detailed balance theory: $\Delta V_{\text{oc}} = \frac{kT}{q} \ln(\text{EQE}_{\text{EL}})$ [33]. With reducing $\Delta E_{\text{CBM-LUMO}}$ offset from 0.98 to -0.02 eV, the resulting EQE_{EL} values of 0.12% (BA-NO₂-2), 0.19% (BA-NO₂-1), 0.45% (BA-OCH₃), 0.87% (pristine), 1.91% (PA-OH) and 5.91% (PA-OCH₃) at J_{sc} correspond to 174.86, 162.91, 140.50, 123.35, 102.91 and 73.54 mV of $\Delta V_{\text{nonrad oc}}$, respectively, indicating that reduction of $\Delta E_{\text{CBM-LUMO}}$ suppresses the nonradiative recombination loss in PSCs. Furthermore, compared to the radiative recombination loss from the S-Q

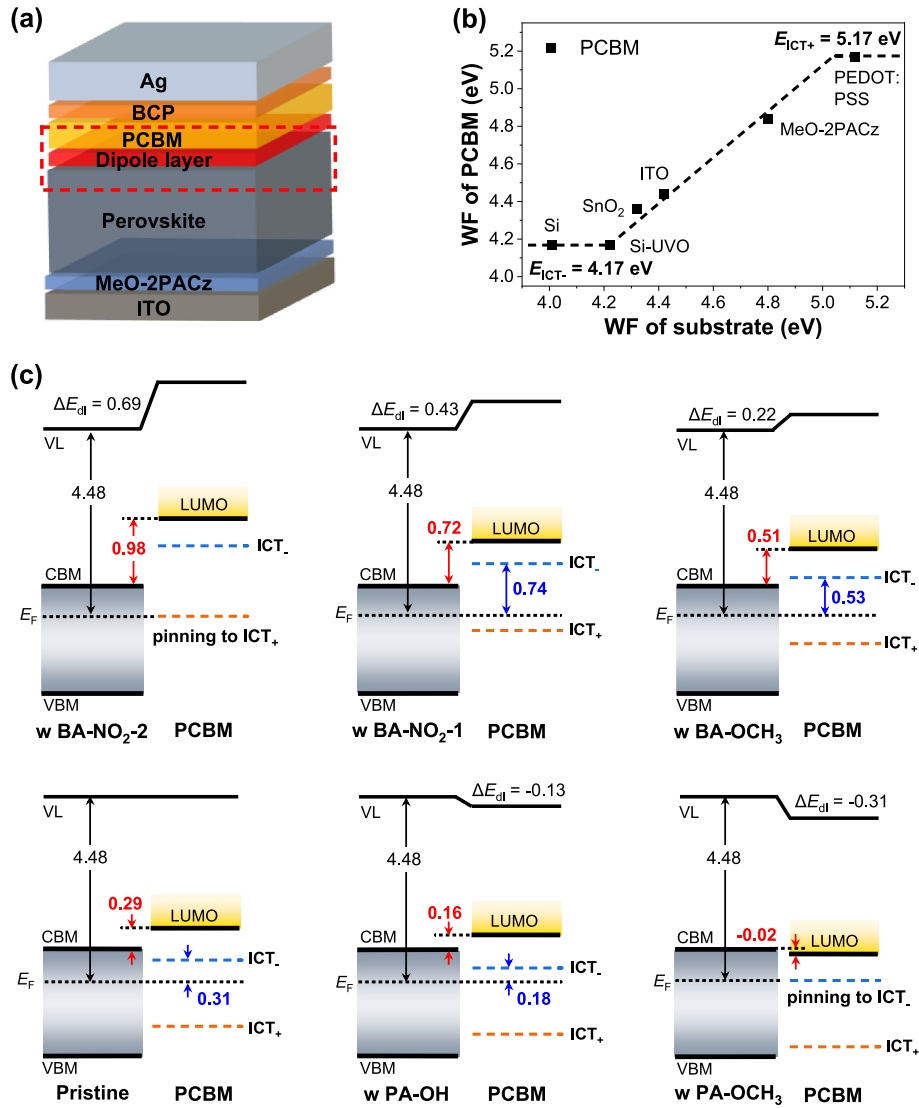


Fig. 2. (a) Architecture of p-i-n PSCs. (b) Dependence of WFs of PCBM films on WFs of bare substrates. (c) UPS-derived energetics of CBM-LUMO energy offset evolution at perovskite/PCBM heterointerfaces with different dipole layers. The heterointerface energetics are tuned over the range between pinning to ICT₊ and pinning to ICT₋.

limit of V_{oc} (1.285 V for PSCs based on 1.55 eV band gap perovskite), it is concluded that the suppressed nonradiative recombination is the main contributor to the enlarged V_{oc} of the device (Fig. 4e), attributed to the matched energetics with the small $\Delta E_{CBM-LUMO}$ at the perovskite/PCBM heterointerface. In addition, the maximum FF (FF_{max}) without charge transport loss is estimated according to the equation: $FF_{max} = \frac{v_{oc} - \ln(v_{oc} + 0.72)}{v_{oc} + 1}$ (where $v_{oc} = \frac{qV_{oc}}{nkT}$) [34]. The calculated FF_{max} rises from 80.91% to 86.34% by reducing $\Delta E_{CBM-LUMO}$, and the charge transport-induced FF loss in the devices decreases significantly from 16.07% to 1.63% (Fig. 4f). These findings are consistent with the suppression of nonradiative recombination and the remarkable improvement of electron extraction efficacy in PSCs with decreased $\Delta E_{CBM-LUMO}$.

3.5. Discussion

To further discuss the importance of $\Delta E_{CBM-LUMO}$ in PSCs, we apply femtosecond transient absorption (fs-TA) spectroscopy to verify the charge transfer dynamics at perovskite/PCBM heterointerface. The photo-bleach (PB) signals of high-WF perovskite/PCBM, moderate (e.g., pristine)-WF perovskite/PCBM, and low-WF

perovskite/PCBM films are fully represented by pseudo-color images, and their TA profiles with different probe delay times are plotted (Fig. S7 online). The decay curves of PB signals are fitted by a bi-exponential decay equation (Fig. 5a and Table S3 online), where the initial fast component can be attributed to charge diffusion in the perovskite bulk, while the slow component corresponds to charge extraction process at perovskite/PCBM heterointerface [35]. The decay time related to charge extraction (τ_e) decreases from 606 ps for the moderate (e.g., pristine)-WF perovskite/PCBM heterointerface to 419 ps for the low-WF perovskite/PCBM heterointerface. The longest charge extraction time of 672 ps is observed at the high-WF perovskite/PCBM heterointerface. The shortest charge extraction time suggests a highly electron-selective contact for the low-WF perovskite/PCBM heterointerface, whereas the longest charge extraction time of the high-WF perovskite/PCBM heterointerface indicates that it suffers from the largest electron extraction barrier. These results are all in agreement with an enhanced electron extraction rate upon reduced $\Delta E_{CBM-LUMO}$.

We summarize our findings on the energetics of the perovskite/PCBM heterointerface and their correlation to the performance of

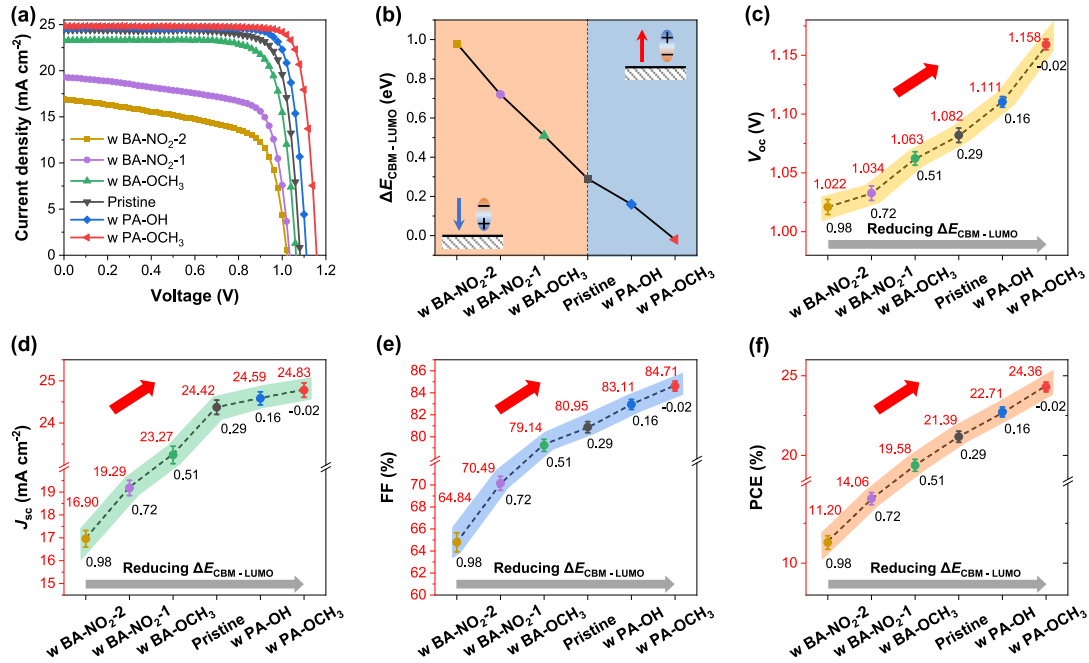


Fig. 3. (a) $J-V$ curves of p-i-n PSCs with different dipole layers. (b) $\Delta E_{\text{CBM-LUMO}}$ values at perovskite/PCBM heterointerface. Diversification of device photovoltaic parameters (c) V_{oc} , (d) J_{sc} , (e) FF and (f) PCE with reducing $\Delta E_{\text{CBM-LUMO}}$.

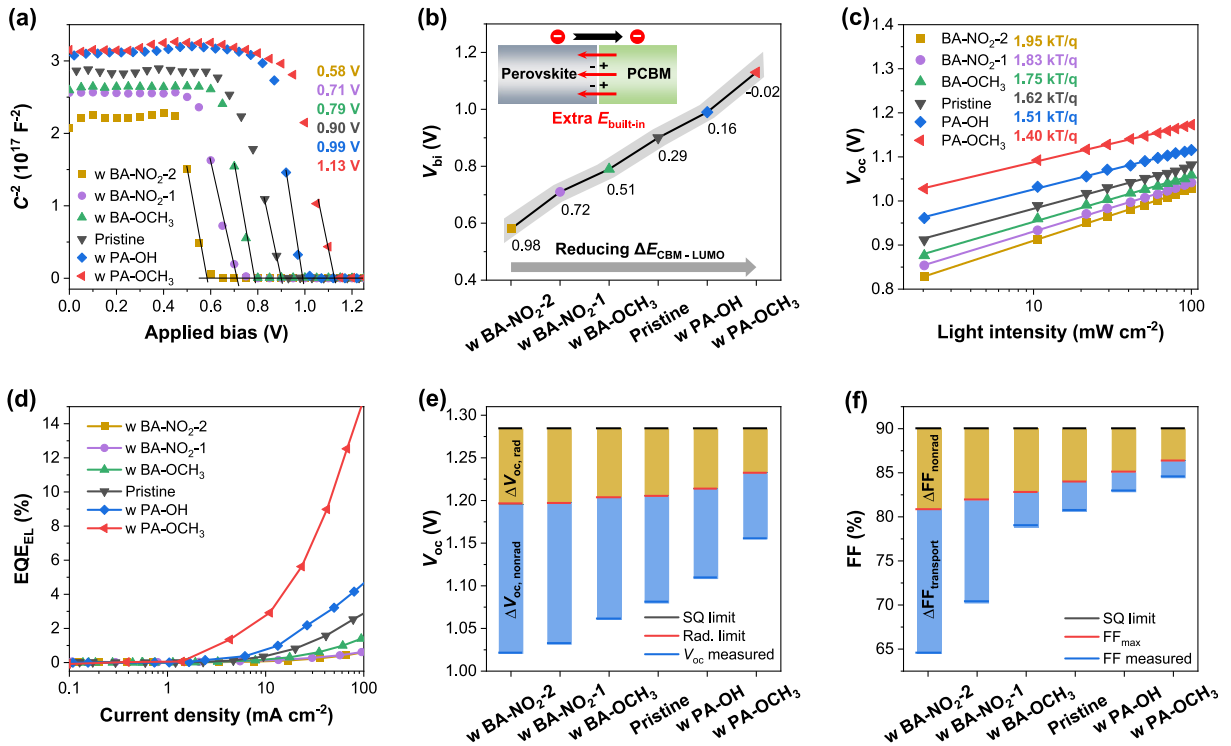


Fig. 4. (a) Mott-Schottky plots of p-i-n PSCs. (b) V_{bi} with reducing $\Delta E_{\text{CBM-LUMO}}$. (c) Dependence of V_{oc} on light intensity. (d) EQE_{EL} spectra under different injection current densities. (e) V_{oc} loss analysis and (f) FF loss analysis of p-i-n PSCs.

p-i-n PSCs, and propose a general energetics model (Fig. 5b). For high-WF perovskite surface (equal to or larger than the E_{ICT^+} of PCBM), the perovskite E_{F} pins to the positive polaron transport state of PCBM at the heterointerface, limiting the maximum $\Delta E_{\text{CBM-LUMO}}$ to 0.98 eV. In this scenario, the poor electron selectivity at the contact will cause severe nonradiative recombination and extensive bimolecular recombination at the interface region,

leading to low PCE with losses in V_{oc} , FF and J_{sc} . The resulting electron accumulation at the heterointerface would also induce device instability due to aggravated halide migration [25]. For low-WF perovskite surfaces (equal to or smaller than the E_{ICT^-} of PCBM), the perovskite E_{F} pins to the negative polaron transport state of PCBM, yielding a minimum achievable $\Delta E_{\text{CBM-LUMO}}$ of -0.02 eV, i.e. barrier-free and hence a highly electron-selective contact that

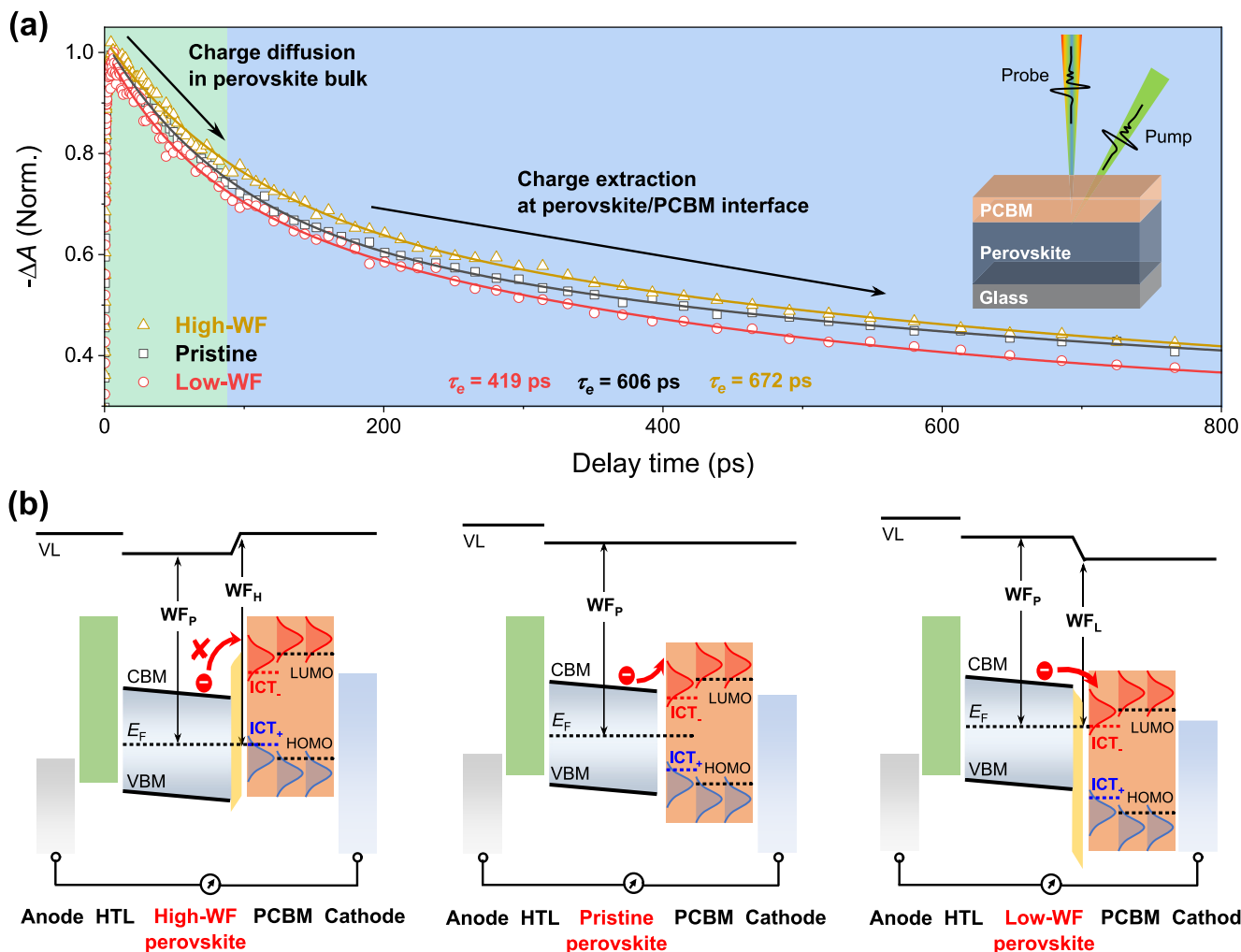


Fig. 5. (a) Charge extraction kinetics at perovskite/PCBM heterointerfaces that feature high-WF perovskite, moderate-WF (e.g., pristine) perovskite, and low-WF perovskite, respectively, extracted from fs-TA results. (b) Proposed energetics models on energy level alignment and electron extraction for p-i-n PSCs.

enhances PCE, V_{oc} , FF and J_{sc} . The decreased electron accumulation at such contacts is expected to also improve the PSC stability. For perovskite surfaces with moderate WF, i.e. where the perovskite E_F lies between the E_{ICT+} and E_{ICT-} of PCBM, they follow the so-called vacuum level alignment regime. In this case, the $\Delta E_{CBM-LUMO}$ will vary between the maximum endpoint and minimum endpoint (0.98 to -0.02 eV) with PSC device parameters affected accordingly.

4. Conclusion

In conclusion, we present comprehensive experimental evidence and theoretical analysis on the correlation between interfacial energetics of perovskite heterojunction and device photovoltaic performance, enabling high-performance p-i-n PSCs. We reconstruct the energy offsets for electron extraction from 0.98 to -0.02 eV by modifying the perovskite surface WF with SAMs inducing surface dipoles, yielding an impressive improvement in efficiency. The improved photovoltaic performance is attributed to the matched energetics with zero energy offset between the perovskite CBM and fullerene electron accepting state, effectively accelerating electron extraction across from perovskite to PCBM and thus suppressing nonradiative recombination. Conversely, energy offsets trigger severe nonradiative recombination, causing significant charge carrier transport losses at such electron-

selective contact. These fundamental insights on the nature and importance of energy level alignment at perovskite charge-selective contacts will assist in further optimizing the performance of multilayer-structural perovskite optoelectronic devices.

Conflict of interest

The authors declare that they have no conflict of interest.

Acknowledgments

This work was supported by the National Natural Science Foundation of China (62322407, 22279034, 52261145698, 52125205, and W2421103), the National Key Research and Development Program of China (2022YFB3803300), and the Shanghai Science and Technology Innovation Action Plan (24110714100, and 22ZR1418900). M. F. and X. L. acknowledge support from the STINT grant (CH2017-7163) and the Swedish Government Strategic Research Area in Materials Science on Functional Materials at Linköping University (Faculty Grant SFO Mat LiU no. 2009 00971).

Author contributions

Qinye Bao conceived the idea and directed the overall project. Shaobing Xiong fabricated the devices, conducted the

characterization and wrote the draft manuscript. Di Li, Junhan Xie, and Bo Li conducted PL/TRPL/TA measurements. Hongbo Wu and Zaifei Ma performed EQ_{EL} measurements. Qinye Bao, Caofeng Pan, Mats Fahlman, Xianjie Liu, and Junhao Chu revised the manuscript. All authors commented on the manuscript.

Appendix A. Supplementary material

Supplementary data to this article can be found online at <https://doi.org/10.1016/j.scib.2025.03.034>.

References

- [1] Yin WJ, Shi T, Yan Y. Unique properties of halide perovskites as possible origins of the superior solar cell performance. *Adv Mater* 2014;26:4653–8.
- [2] Yang Z, Surrente A, Galkowski K, et al. Unraveling the exciton binding energy and the dielectric constant in single-crystal methylammonium lead triiodide perovskite. *J Phys Chem Lett* 2017;8:1851–5.
- [3] Xing G, Mathews N, Sun S, et al. Long-range balanced electron- and hole-transport lengths in organic inorganic $CH_3NH_3PbI_3$. *Science* 2013;342:344.
- [4] Eperon GE, Stranks SD, Menelaou C, et al. Formamidinium lead trihalide: a broadly tunable perovskite for efficient planar heterojunction solar cells. *Energy Environ Sci* 2014;7:982–8.
- [5] Reddy SH, Di Giacomo F, Di Carlo A. Low-temperature-processed stable perovskite solar cells and modules: a comprehensive review. *Adv Energy Mater* 2022;12:2103534.
- [6] Xiong S, Bao Q, Chu J. Recent progress on natural biomaterials boosting high-performance perovskite solar cells. *J Infrared Millim Waves* 2022;41:517.
- [7] Wolff CM, Caprioglio P, Stolterfoht M, et al. Nonradiative recombination in perovskite solar cells: the role of interfaces. *Adv Mater* 2019;31:1902762.
- [8] Luo D, Su R, Zhang W, et al. Minimizing non-radiative recombination losses in perovskite solar cells. *Nat Rev Mater* 2020;5:44–60.
- [9] Warby J, Zu F, Zeiske S, et al. Understanding performance limiting interfacial recombination in pin perovskite solar cells. *Adv Energy Mater* 2022;12:2103567.
- [10] Stolterfoht M, Caprioglio P, Wolff CM, et al. The impact of energy alignment and interfacial recombination on the internal and external open-circuit voltage of perovskite solar cells. *Energy Environ Sci* 2019;12:2778–88.
- [11] Yang J, Xiong S, Song J, et al. Energetics and energy loss in 2D Ruddlesden-Popper perovskite solar cells. *Adv Energy Mater* 2020;10:2000687.
- [12] Xiong S, Jiang S, Zhang Y, et al. Revealing buried heterointerface energetics towards highly efficient perovskite solar cells. *Nano Energy* 2023;109:108281.
- [13] Lu Y, Zhong J, Yu Y, et al. Constructing an n/n⁺ homojunction in a monolithic perovskite film for boosting charge collection in inverted perovskite photovoltaics. *Energy Environ Sci* 2021;14:4048–58.
- [14] Xiong S, Hou Z, Dong W, et al. Additive-induced synergies of defect passivation and energetic modification toward highly efficient perovskite solar cells. *Adv Energy Mater* 2021;11:2101394.
- [15] Zheng X, Hou Y, Bao C, et al. Managing grains and interfaces via ligand anchoring enables 22.3%-efficiency inverted perovskite solar cells. *Nat Energy* 2020;5:131–40.
- [16] Liu Y, Dong B, Hagfeldt A, et al. Chemically tailored molecular surface modifiers for efficient and stable perovskite photovoltaics. *SmartMat* 2021;2:33–7.
- [17] Liu C, Yang Y, Chen H, et al. Bimolecularly passivated interface enables efficient and stable inverted perovskite solar cells. *Science* 2023;382:810–5.
- [18] He R, Wang W, Yi Z, et al. Improving interface quality for 1-cm² all-perovskite tandem solar cells. *Nature* 2023;618:80–6.
- [19] Zhang S, Ye F, Wang X, et al. Minimizing buried interfacial defects for efficient inverted perovskite solar cells. *Science* 2023;380:404–9.
- [20] Park SM, Wei M, Lempeis N, et al. Low-loss contacts on textured substrates for inverted perovskite solar cells. *Nature* 2023;624:289–94.
- [21] Li Z, Sun X, Zheng X, et al. Stabilized hole-selective layer for high-performance inverted p-i-n perovskite solar cells. *Science* 2023;382:284–9.
- [22] Siekmann J, Kulkarni A, Akel S, et al. Characterizing the influence of charge extraction layers on the performance of triple-cation perovskite solar cells. *Adv Energy Mater* 2023;13:2300448.
- [23] Warby J, Shah S, Thiesbrummel J, et al. Mismatch of quasi-Fermi level splitting and V_{oc} in perovskite solar cells. *Adv Energy Mater* 2023;13:2303135.
- [24] Jiang Q, Zhao Y, Zhang X, et al. Surface passivation of perovskite film for efficient solar cells. *Nat Photonics* 2019;13:460–6.
- [25] Tan S, Huang T, Yavuz I, et al. Stability-limiting heterointerfaces of perovskite photovoltaics. *Nature* 2022;605:268–73.
- [26] Lee J-W, Tan S, Seok SI, et al. Rethinking the A cation in halide perovskites. *Science* 2022;375:eabj1186.
- [27] Canil L, Cramer T, Fraboni B, et al. Tuning halide perovskite energy levels. *Energy Environ Sci* 2021;14:1429–38.
- [28] Bao Q, Sandberg O, Dagnelund D, et al. Trap-assisted recombination via integer charge transfer states in organic bulk heterojunction photovoltaics. *Adv Funct Mater* 2014;24:6309–16.
- [29] Aarnio H, Sehati P, Braun S, et al. Spontaneous charge transfer and dipole formation at the interface between P3HT and PCBM. *Adv Energy Mater* 2011;1:792–7.
- [30] Bao Q, Liu X, Braun S, et al. Oxygen- and water-based degradation in [6,6]-phenyl-C61-butyric acid methyl ester (PCBM) films. *Adv Energy Mater* 2014;4:1301272.
- [31] Zang X, Xiong S, Jiang S, et al. Passivating dipole layer bridged 3D/2D perovskite heterojunction for highly efficient and stable p-i-n solar cells. *Adv Mater* 2024;36:2309991.
- [32] Fu S, Li X, Wan L, et al. Efficient passivation with lead pyridine-2-carboxylic for high-performance and stable perovskite solar cells. *Adv Energy Mater* 2019;9:1901852.
- [33] Yang G, Ren Z, Liu K, et al. Stable and low-photovoltage-loss perovskite solar cells by multifunctional passivation. *Nat Photonics* 2021;15:681–9.
- [34] Jeong MJ, Moon CS, Lee S, et al. Boosting radiation of stacked halide layer for perovskite solar cells with efficiency over 25%. *Joule* 2023;7:112–27.
- [35] Hung C, Mai C, Wu C, et al. Self-assembled monolayers of bi-functionalized porphyrins: a novel class of hole-layer-coordinating perovskites and indium tin oxide in inverted solar cells. *Angew Chem, Int Ed* 2023;62:e202309831.